

Low-Bandgap Se-Deficient Antimony Selenide as a Multifunctional Polysulfide Barrier toward High-Performance Lithium–Sulfur Batteries

Yuan Tian, Gaoran Li, Yongguang Zhang,* Dan Luo, Xin Wang, Yan Zhao, Hui Liu, Puguang Ji, Xiaohang Du, Jingde Li,* and Zhongwei Chen*

The shuttling behavior and sluggish conversion kinetics of the intermediate lithium polysulfides (LiPSs) represent the main obstructions to the practical application of lithium–sulfur (Li–S) batteries. Herein, an anion-deficient design of antimony selenide ($\text{Sb}_2\text{Se}_{3-x}$) is developed to establish a multifunctional LiPS barrier toward the inhibition of polysulfide shuttling and enhancement of battery performance. The defect chemistry in the as-developed $\text{Sb}_2\text{Se}_{3-x}$ promotes the intrinsic conductivity, strengthens the chemical affinity to LiPSs, and catalyzes the sulfur electrochemical conversion, which are verified by a series of computational and experimental results. Attributed to these unique superiorities, the obtained LiPS barrier efficiently promotes and stabilizes the sulfur electrochemistry, thus enabling excellent Li–S battery performance, e.g., outstanding cyclability over 500 cycles at 1.0 C with a minimum capacity fading rate of 0.027% per cycle, a superb rate capability up to 8.0 C, and a high areal capacity of 7.46 mAh cm⁻² under raised sulfur loading. This work offers a defect engineering strategy toward fast and durable sulfur electrochemistry, holding great promise in developing practically viable Li–S batteries as well as enlightening the material design of related energy storage and conversion systems.

Benefiting from the intriguingly high energy density up to 2600 Wh kg⁻¹, lithium–sulfur (Li–S) batteries have attracted extensive research interest for the development of advanced energy storage technology that outperforms state-of-the-art lithium-ion batteries.^[1,2] Moreover, the natural abundance and nontoxic nature of the element sulfur lead to economic benefits and environmental benignity, which particularly favor large-scale applications.^[3] Despite the convincing merits, the practical implementation of Li–S batteries still suffers from several intractable technical challenges, such as the electrical resistivity of sulfur, the dissolution of lithium polysulfides (LiPSs) with a severe “shuttle effect,” and the large volume variation during battery cycling, which seriously hinder this technology from yielding practically viable energy density and cyclability.^[4–7]

In response to these obstructions, the development of functional separators has emerged as a promising strategy to confine the sulfur species within the cathodic chamber, thus realizing effective inhibition of polysulfide shuttling and enhancement of the battery performance.^[8–12] Such a barrier against LiPS penetration is also expected to protect the lithium anode from detrimental attacks that cause surface passivation.^[13,14] Previous studies following this concept have mainly focused on materials such as porous carbon materials, metal oxides/sulfides and their composites, which are uniformly coated on the cathodic surface of the separator to physically and chemically trap LiPSs.^[15–19] This combined adsorption mechanism has shown considerable capability for stabilizing the sulfur electrochemistry and enhancing sulfur utilization in Li–S batteries, whereas the LiPS conversion is still restricted by its intrinsically sluggish kinetics and the low conductivity of oxides/sulfides. Recent studies have revealed the great capability of defect engineering in tailoring the electronic structures of these polar inorganics toward enhanced conductive features as well as interactive affinity to certain species, which offers a promising approach to concurrently realize strong sulfur confinement and expedite the LiPS conversion in Li–S systems.^[20,21] Despite the considerable research efforts on O- or S-deficient metal chalcogenides, the studies on Se-deficient

Y. Tian, Prof. Y. Zhang, Y. Zhao, Prof. H. Liu, Prof. P. Ji
School of Materials Science and Engineering
Tianjin Key Laboratory of Materials Laminating Fabrication and Interface
Control Technology

Hebei University of Technology
Tianjin 300130, China
E-mail: yongguangzhang@hebut.edu.cn

Dr. G. Li, D. Luo, Prof. Z. Chen
Department of Chemical Engineering
University of Waterloo
Waterloo, ON N2L 3G1, Canada
E-mail: zhwchen@uwaterloo.ca

Prof. X. Wang
International Academy of Optoelectronics at Zhaoqing
South China Normal University
Guangdong 510631, China

Dr. X. Du, Prof. J. Li
National–Local Joint Engineering Laboratory for Energy Conservation
of Chemical Process Integration and Resources Utilization
School of Chemical Engineering and Technology
Hebei University of Technology
Tianjin 300130, China
E-mail: jingdeli@hebut.edu.cn

 The ORCID identification number(s) for the author(s) of this article can be found under <https://doi.org/10.1002/adma.201904876>.

DOI: 10.1002/adma.201904876

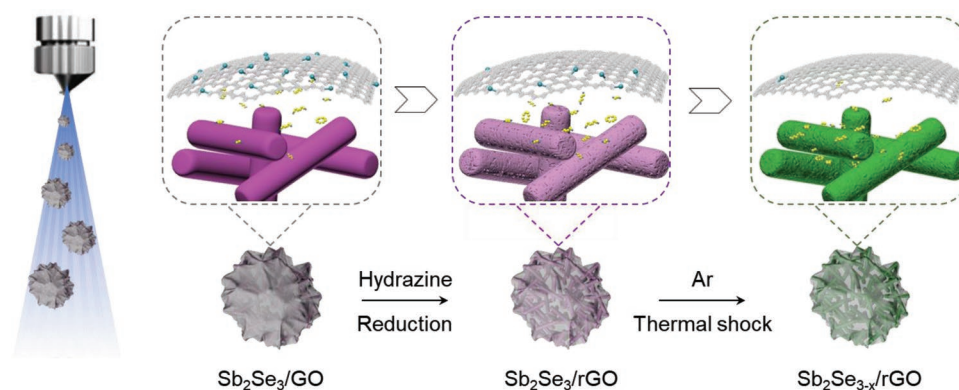


Figure 1. Schematic illustration of the synthetic procedure for the $\text{Sb}_2\text{Se}_{3-x}/\text{rGO}$ microspheres.

selenides are still very limited in Li–S batteries. Generally, selenides deliver considerable semiconductivity with higher potential for electrochemical applications compared with oxides and sulfides. Among them, antimony selenide (Sb_2Se_3) as a low-cost, relatively earth-abundant, and low-bandgap (1.0–1.2 eV) semiconductor has been widely studied as a good light absorber in solar cells.^[22,23] More importantly, the phase and defects in Sb_2Se_3 can easily be controlled to potentially meet the specific requirements for the improvement of Li–S battery systems.^[24,25]

Herein, we developed a hierarchical composite (denoted $\text{Sb}_2\text{Se}_{3-x}/\text{rGO}$) with defect-rich $\text{Sb}_2\text{Se}_{3-x}$ nanorods wrapped by reduced graphene oxide (rGO) to establish a multifunctional LiPS barrier toward improved Li–S battery performance. The spray-drying method was employed to construct the hierarchical structure with robust integrity and long-range charge transfer pathways, while the subsequent chemical reduction and thermal shock introduced abundant Se vacancies (V_{Se}) into the product $\text{Sb}_2\text{Se}_{3-x}/\text{rGO}$ composite. The correlation between the defect chemistry and the electrochemical improvements was comprehensively and convincingly studied. The defect engineering not only endows $\text{Sb}_2\text{Se}_{3-x}$ with enhanced conductivity compared with its parent material but also strengthens its chemical adsorption to LiPSs, as verified by a series of experimental and computational results. In addition, such defect design also significantly promotes the LiPS conversion reactions, thus realizing a simultaneously conductive, adsorptive and catalytic barrier against polysulfide shuttling as well as the resultant fast and durable sulfur electrochemistry. Attributed to these advantageous features, the implementation of the $\text{Sb}_2\text{Se}_{3-x}/\text{rGO}$ -modified separator in Li–S cells enables a superb rate capability up to 8.0 C, excellent cyclic stability with a low capacity fading of 0.027% per cycle under 1.0 C, and a high areal capacity of 7.46 mAh cm^{-2} under a raised sulfur loading of 8.1 mg cm^{-2} . To the best of our knowledge, this is the first report on Se-deficient metal selenide for improvement of the Li–S configuration, which pioneers a new way for defect engineering in pursuit of high-efficiency sulfur electrochemistry as well as high-performance Li–S batteries.

$\text{Sb}_2\text{Se}_{3-x}/\text{rGO}$ hierarchical porous microspheres were fabricated through a facile and scalable spray-drying approach followed by chemical reduction to introduce V_{Se} and by thermal

shock to further increase the V_{Se} content (**Figure 1**). $\text{Sb}_2\text{Se}_{3-x}$ nanorods were first prepared by a solution-based method as previously reported (see details in the Experimental Section).^[26] Scanning electron microscopy (SEM) and transmission electron microscopy (TEM) images confirm the uniform morphology and size distribution of the obtained Sb_2Se_3 with a diameter of ≈ 100 nm (**Figure 2a,b**). In addition, the high-resolution TEM (HRTEM) image manifests the highly crystalline nature by showing a clear lattice fringe with a d -spacing of 0.372 nm, which can be assigned to the (130) plane in the orthorhombic Sb_2Se_3 crystal (inset in **Figure 2b**). Subsequently, spray drying and chemical reduction were performed to yield the $\text{Sb}_2\text{Se}_3/\text{rGO}$ composite, which was further subjected to thermal shock to achieve $\text{Sb}_2\text{Se}_{3-x}/\text{rGO}$. Both the as-prepared $\text{Sb}_2\text{Se}_3/\text{rGO}$ and $\text{Sb}_2\text{Se}_{3-x}/\text{rGO}$ exhibit uniform microspherical primary structures with a diameter of ≈ 4 μm and a considerable number of nanorods wrapped by rGO nanosheets (**Figure 2c–e**; **Figure S1**, Supporting Information). Elemental mappings confirm the uniform distribution of Sb, Se, and C in both the $\text{Sb}_2\text{Se}_3/\text{rGO}$ and $\text{Sb}_2\text{Se}_{3-x}/\text{rGO}$ composites. The intimate contact between the wrinkled rGO nanosheets and $\text{Sb}_2\text{Se}_{3-x}$ nanorods is expected to facilitate Li^+ and electron transfer and maintain a robust structural integrity, thus favoring fast and stable electrochemical processes. The crystalline feature of $\text{Sb}_2\text{Se}_{3-x}$ was investigated by HRTEM and the fast Fourier transform (FFT) pattern (**Figure 2f** and inset), which confirms the well-maintained crystallinity of orthorhombic Sb_2Se_3 as well as the tight wrapping by rGO. Notably, relatively disordered lattices can be perceived in the inverse FFT (IFFT) image (**Figure 2g**, yellow frame) due to the emergence of low-valence Sb on the surface induced by the thermal shock, while the inner Sb_2Se_3 maintains a relatively perfect crystalline structure.^[27] These disordered structures are expected to provide trapping sites for charge carriers and interfere with their rapid recombination to improve the electron transfer efficiency.^[28] The lattice spacing profile comparison between the disordered (**Figure 2h**, yellow frame) and perfect crystalline (pink frame) structures further confirms the defective nature of the obtained $\text{Sb}_2\text{Se}_{3-x}$ by showing a slightly expanded interplanar spacing on the (130) face. High-magnification elemental mapping was also performed at a selected area, as shown in **Figure 2i–l**, which further demonstrates the homogeneous element distribution as well as the wrapping structure of the obtained $\text{Sb}_2\text{Se}_{3-x}/\text{rGO}$ composite.

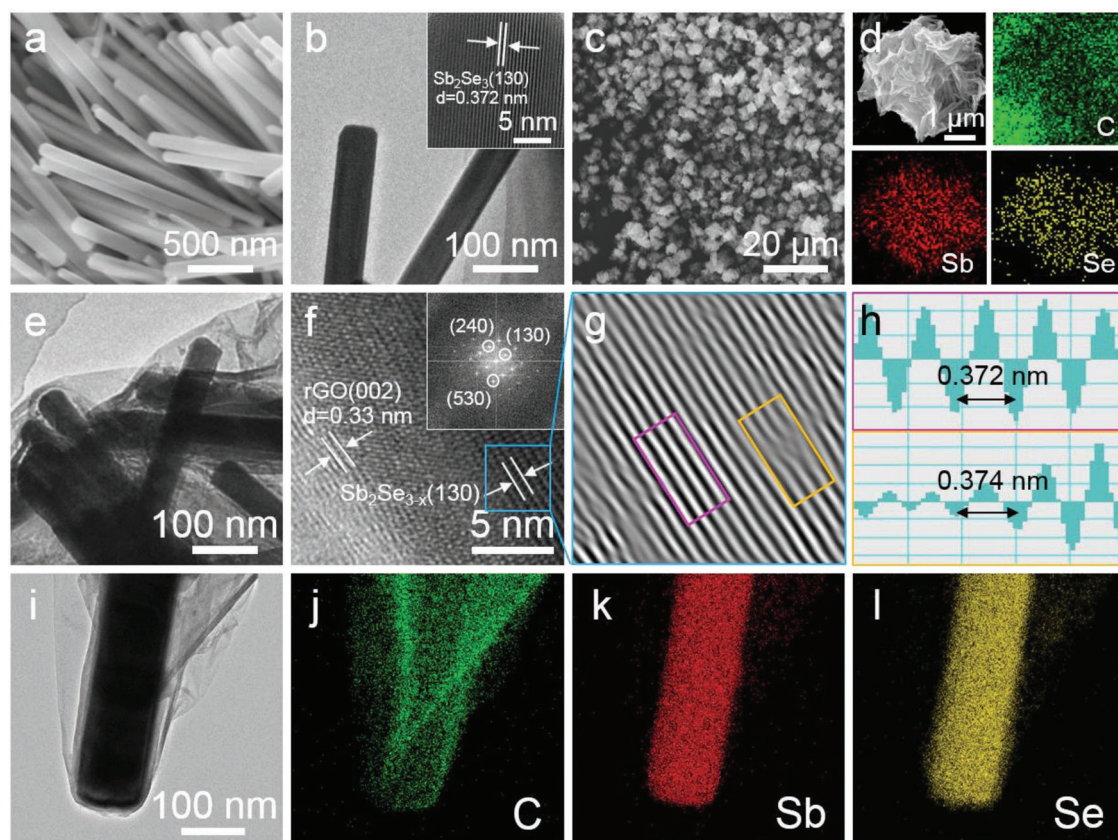


Figure 2. a) SEM, b) TEM and HRTEM (inset) images of Sb_2Se_3 nanorods; c) SEM image and d) elemental mapping of $\text{Sb}_2\text{Se}_{3-x}/\text{rGO}$ microspheres; e) TEM image, f) HRTEM image and FFT pattern at the selected area in blue (inset), g) inverse FFT lattice image, h) lattice spacing profiles at selected areas in pink and yellow, and i–l) high-magnification elemental mapping of $\text{Sb}_2\text{Se}_{3-x}/\text{rGO}$ microspheres.

The physiochemical properties of the obtained materials were studied and compared to reveal the potential structural superiorities of the defective $\text{Sb}_2\text{Se}_{3-x}/\text{rGO}$. The crystalline structures of Sb_2Se_3 , $\text{Sb}_2\text{Se}_3/\text{rGO}$ and $\text{Sb}_2\text{Se}_{3-x}/\text{rGO}$ were investigated by X-ray diffraction (XRD), as shown in **Figure 3a**. Both $\text{Sb}_2\text{Se}_3/\text{rGO}$ and $\text{Sb}_2\text{Se}_{3-x}/\text{rGO}$ exhibit a group of sharp diffraction peaks that well match the orthorhombic Sb_2Se_3 with the space group of $Pbnm$ 62 (JCPDS No. 15-0861), indicating that their crystallized structure is consistent with the HRTEM results. Meanwhile, a broad peak can be observed at 26.3° corresponding to the (002) plane of rGO.^[29,30] Interestingly, the magnified observation of the XRD patterns reveals a peak downshift for $\text{Sb}_2\text{Se}_{3-x}/\text{rGO}$, especially in the small angle range (Figure S2, Supporting Information). Meanwhile, the Raman spectra (Figure 3b) in the low wavenumber range also show a continuous upshift of the peaks at ≈ 189 and 252 cm^{-1} , which are assigned to the heteropolar Sb–Se and nonpolar Sb–Sb vibrations, respectively, from Sb_2Se_3 to $\text{Sb}_2\text{Se}_3/\text{rGO}$ and $\text{Sb}_2\text{Se}_{3-x}/\text{rGO}$. These variations originate from the atomic rearrangement and reconstruction of Sb_2Se_3 that partially alters the Se–Sb–Se bond length as well as the corresponding crystal lattice parameters (Table S1, Supporting Information), signifying the formation as well as increase of V_{Se} in the obtained materials upon the defect introduction process.^[31–33] Further evidence can be obtained from the electron paramagnetic response (EPR) spectra, as shown in Figure 3c. In contrast to the flat spectrum

of Sb_2Se_3 , $\text{Sb}_2\text{Se}_3/\text{rGO}$ exhibits a considerable EPR signal with a g -value of 2.00, which corresponds to the unpaired electrons induced by the partial removal of Se.^[34,35] This signal is further intensified in the EPR profile of $\text{Sb}_2\text{Se}_{3-x}/\text{rGO}$, confirming the increase of V_{Se} after the thermal shock. The removal of Se is expected to induce a redistribution of the excess electrons among the nearest neighboring atoms to form shallow donor states. These effects are considered favorable for conductivity enhancement of the V_{Se} -rich $\text{Sb}_2\text{Se}_{3-x}/\text{rGO}$, which is confirmed by the density of states (DOS), as shown in Figure 3d. Sb_2Se_3 and $\text{Sb}_2\text{Se}_{3-x}$ show a clear energy gap for spin-up and spin-down channels with a typical semiconducting character, while the Fermi level (dashed line) is located at the top of the valence band. Importantly, the DOS pattern of $\text{Sb}_2\text{Se}_{3-x}$ reveals a considerable state rearrangement from Sb_2Se_3 along with the emergence of a shallow donor level (defect level). Electrons below the Fermi level can leap into the defect level, which creates a hole carrier and lowers the barrier of electron transition to the conduction band, thus contributing to the enhanced conductivity (Figure S3, Supporting Information).^[36] Additionally, the lower $I_{\text{D}}/I_{\text{G}}$ ratio of $\text{Sb}_2\text{Se}_{3-x}/\text{rGO}$ compared with that of $\text{Sb}_2\text{Se}_3/\text{rGO}$ in the Raman spectra (0.88 vs 1.21) suggests a higher graphitization of $\text{Sb}_2\text{Se}_{3-x}/\text{rGO}$, which further benefits the conductivity of the product composite (Figure 3e). Benefiting from these contributions, the as-developed $\text{Sb}_2\text{Se}_{3-x}/\text{rGO}$ shows a significantly higher conductivity of $6.25 \times 10^4\text{ S m}^{-1}$

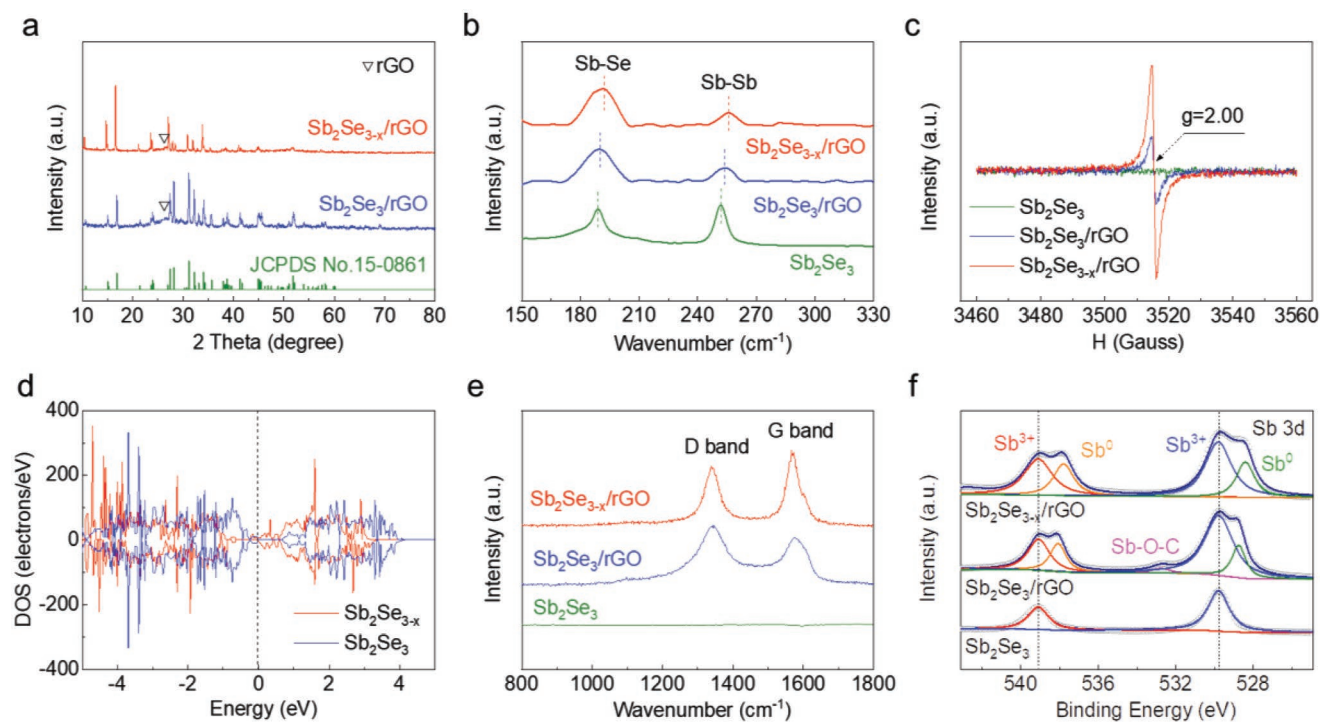


Figure 3. a) XRD patterns, b,e) Raman spectra, and c) EPR spectra of Sb_2Se_3 , $\text{Sb}_2\text{Se}_3/\text{rGO}$ and $\text{Sb}_2\text{Se}_{3-x}/\text{rGO}$; d) DOS of Sb_2Se_3 and $\text{Sb}_2\text{Se}_{3-x}$; f) Sb 3d high-resolution XPS spectra of Sb_2Se_3 , $\text{Sb}_2\text{Se}_3/\text{rGO}$, and $\text{Sb}_2\text{Se}_{3-x}/\text{rGO}$.

than those of Sb_2Se_3 ($6.06 \times 10^{-4} \text{ S m}^{-1}$) and $\text{Sb}_2\text{Se}_3/\text{rGO}$ ($1.23 \times 10^3 \text{ S m}^{-1}$) (Figure S4, Supporting Information), holding great promise in promoting electrochemical sulfur reactions.

The chemical states of Sb_2Se_3 , $\text{Sb}_2\text{Se}_3/\text{rGO}$ and $\text{Sb}_2\text{Se}_{3-x}/\text{rGO}$ were further analyzed by X-ray photoelectron spectroscopy (XPS). The atomic compositions of different samples are summarized in Table S2 (Supporting Information). A continuous decrease in the Se to Sb atomic ratio can be perceived from Sb_2Se_3 to $\text{Se}_2\text{Se}_3/\text{rGO}$ and $\text{Se}_2\text{Se}_{3-x}/\text{rGO}$, which confirms the increase in Se deficiency upon defect introduction. Figure 3f shows the high-resolution XPS spectra for the Sb 3d core levels of Sb_2Se_3 , $\text{Sb}_2\text{Se}_3/\text{rGO}$ and $\text{Sb}_2\text{Se}_{3-x}/\text{rGO}$. Two typical peaks can be observed in the Sb_2Se_3 Sb 3d spectrum at 539.1 and 529.8 eV, corresponding to the $3d_{3/2}$ and $3d_{5/2}$ levels of Sb^{3+} , respectively.^[37] In comparison, $\text{Sb}_2\text{Se}_3/\text{rGO}$ shows a pair of new peaks at 538.0 and 528.7 eV, corresponding to the $3d_{3/2}$ and $3d_{5/2}$ levels of Sb^0 , while these peaks shift to a lower binding energy (BE) range in the spectrum of $\text{Sb}_2\text{Se}_{3-x}/\text{rGO}$. Additionally, a new small peak arises at 532.8 eV in the $\text{Sb}_2\text{Se}_3/\text{rGO}$ composite, which can be assigned to the Sb—O—C bonding originating from the interaction between Sb_2Se_3 and the residual oxygen-containing functional groups in rGO. After subsequent thermal shock, this peak disappears in $\text{Sb}_2\text{Se}_{3-x}/\text{rGO}$, which is consistent with the further reduction of the composite. These variations strongly indicate increasingly higher electron cloud densities as well as lower valence states for Sb from Sb_2Se_3 to $\text{Sb}_2\text{Se}_3/\text{rGO}$ and $\text{Sb}_2\text{Se}_{3-x}/\text{rGO}$ in accordance with the increase of V_{Se} .^[34,38] Moreover, the Se 3d XPS spectra of Sb_2Se_3 , $\text{Sb}_2\text{Se}_3/\text{rGO}$ and $\text{Sb}_2\text{Se}_{3-x}/\text{rGO}$ are also presented in Figure S5 (Supporting Information). The two typical peaks at 55.18 and

54.3 eV are ascribed to the $3d_{3/2}$ and $3d_{5/2}$ levels of Se^{2-} , respectively.^[39] In contrast, a new Se^0 peak emerges at 56.4 eV for $\text{Sb}_2\text{Se}_3/\text{rGO}$, which shifts to a higher BE range (56.6 eV) in $\text{Sb}_2\text{Se}_{3-x}/\text{rGO}$. This result confirms the introduction and increase of Se defects with the chemical reduction and thermal shock processes, which is consistent with the above results.

Given these results, $\text{Sb}_2\text{Se}_{3-x}/\text{rGO}$ with different defect levels was prepared by varying the thermal shock time (denoted 0- $\text{Sb}_2\text{Se}_{3-x}/\text{rGO}$, 2- $\text{Sb}_2\text{Se}_{3-x}/\text{rGO}$, 5- $\text{Sb}_2\text{Se}_{3-x}/\text{rGO}$, 7- $\text{Sb}_2\text{Se}_{3-x}/\text{rGO}$ and 10- $\text{Sb}_2\text{Se}_{3-x}/\text{rGO}$, see details in the Experimental Section) to investigate the influence of V_{Se} on the crystalline and compositional properties of the products. The XRD results show a phase transition from orthorhombic to amorphous with increasing thermal shock time, suggesting continuous destruction of the crystallographic integrity of Sb_2Se_3 and an increase of V_{Se} , which could finally result in structural collapse (Figure S6a, Supporting Information). The conductivities of this series of $\text{Sb}_2\text{Se}_{3-x}/\text{rGO}$ were compared, as shown in Figure S6b (Supporting Information). The results show a significantly enhanced conductivity from 0- $\text{Sb}_2\text{Se}_{3-x}/\text{rGO}$ ($1.23 \times 10^3 \text{ S m}^{-1}$) to 5- $\text{Sb}_2\text{Se}_{3-x}/\text{rGO}$ ($6.25 \times 10^4 \text{ S m}^{-1}$) attributed to the increase of V_{Se} that favors the motion of free electrons, whereas 7- and 10- $\text{Sb}_2\text{Se}_{3-x}/\text{rGO}$ exhibit drastic conductivity declines to 1.98×10^2 and $1.67 \times 10^2 \text{ S m}^{-1}$, respectively, ascribed to structural collapse. Moreover, the continuous decrease in the peak area ratio of Sb^{3+} to Sb^0 also consistently confirms the raised defect level with the extension of the thermal shock treatment time (Figure S6c, Supporting Information). Thus, we employed 5- $\text{Sb}_2\text{Se}_{3-x}/\text{rGO}$ as the optimally defective sample for further investigations.

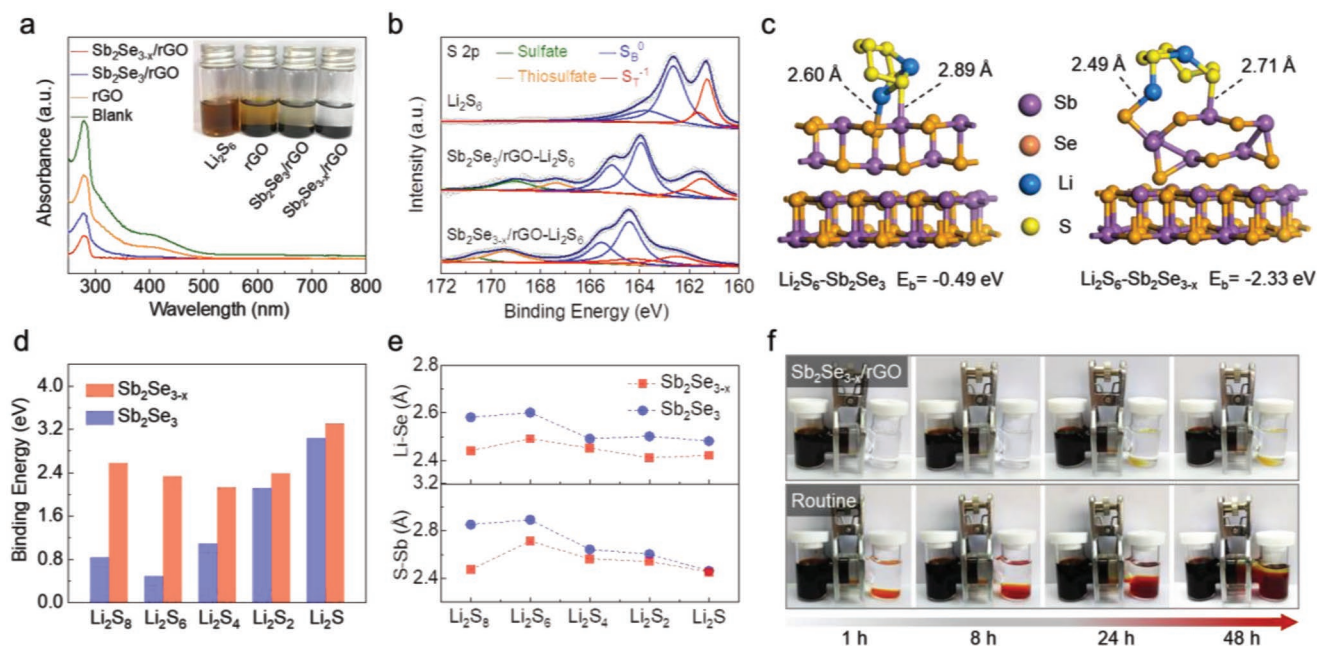


Figure 4. a) Optical observation of LiPS adsorption by rGO, Sb₂Se₃/rGO, and Sb₂Se_{3-x}/rGO after 24 h and the corresponding UV-vis spectra of the supernatants; b) S 2p high-resolution XPS spectra of Li₂S₆, Sb₂Se₃/rGO-Li₂S₆ and Sb₂Se_{3-x}/rGO-Li₂S₆ composites; c–e) DFT calculation results of optimized geometrical configurations of Li₂S₆ (c), BEs (d), and Li–Se and S–Sb bond distances of various LiPS (e) on Sb₂Se₃ and Sb₂Se_{3-x} (130) surfaces; f) LiPS diffusion in H-type cells with Sb₂Se_{3-x}/rGO-modified and routine separators.

These unique features introduced by defect engineering are expected to deliver strong interactions with LiPS species, which favors strong sulfur confinement when these materials are implemented as a functional barrier in Li–S battery configurations. The adsorptive effect was first investigated via optical observation by immersing the same amount of rGO, Sb₂Se₃/rGO and Sb₂Se_{3-x}/rGO into a 10×10^{-3} M Li₂S₆ solution and letting it rest for 24 h. As shown in Figure 4a, in the static adsorption comparison, the solution with Sb₂Se_{3-x}/rGO exhibits the most transparent color, intuitively indicating its strongest adsorption capability for the LiPS. This character is further confirmed by the UV-vis spectra, which show the lowest LiPS-related absorbance peaks in the Sb₂Se_{3-x}/rGO spectrum,^[40] indicating the least amount of LiPS residue in the supernatant and the greatest adsorbability of Sb₂Se_{3-x}/rGO. Additionally, XPS analysis was also performed to reveal the underlying chemical interactions between the LiPS and the adsorbents. As shown in Figure 4b, pristine Li₂S₆ exhibits two pairs of peaks located at 161.3 and 163.8 eV, ascribed to the terminal (S_T⁻¹) and bridging (S_B⁰) sulfur, respectively. After interacting with Sb₂Se₃/rGO, a significant shift of these peaks toward a higher BE range can be perceived, suggesting a reduction in the electron cloud density of sulfur atoms attributed to the chemical adsorption by Sb₂Se₃/rGO. Meanwhile, two new broad peaks appear in the high BE region, which can be assigned to the formation of sulfate (169.1 eV) and thiosulfate (167.4 eV).^[41] In addition, the interaction between the LiPS and Sb₂Se_{3-x}/rGO leads to a more significant peak shift compared with that for Sb₂Se₃/rGO, indicating its higher chemical affinity to the LiPS that favors stronger sulfur confinement in the corresponding Li–S batteries. In addition, the interactive chemistry can also be supported by the Li 1s spectra, as shown in Figure S7

(Supporting Information). The pristine Li₂S₆ displays a typical peak at 55.3 eV, corresponding to the Li–S bond. However, a new peak emerges at 54.5 eV after adsorption by Sb₂Se₃/rGO, which further shifts to a lower BE for the Sb₂Se_{3-x}/rGO-Li₂S₆ composite, suggesting the formation of a “lithium-bond”-like configuration that bridges the adsorber and LiPS as well as an enhanced adsorbability due to the increase of V_{Se} in Sb₂Se_{3-x}.^[42] Furthermore, the interactive chemistry between the as-developed materials and LiPS was verified by density functional theory (DFT) calculations. The geometrically stable configurations of Li₂S₆-Sb₂Se₃ and Li₂S₆-Sb₂Se_{3-x} are illustrated in Figure 4c. The results reveal that the S and Li atoms in Li₂S₆ prefer to bond with the Sb and Se atoms on the Sb₂Se_{3-x} (130) surface, respectively, which is consistent with the XPS analysis. The shorter bond length of S–Sb (2.71 vs 2.89 Å) and Li–Se (2.49 vs 2.60 Å) in the Li₂S₆-Sb₂Se_{3-x} couple compared with those in Li₂S₆-Sb₂Se₃ confirms the higher chemical affinity of V_{Se}-rich Sb₂Se_{3-x} to the LiPS. As a result, a significantly higher BE of –2.33 eV is achieved for Li₂S₆-Sb₂Se_{3-x} than for Li₂S₆-Sb₂Se₃ (–0.49 eV). Furthermore, computational simulations of the interactions between Sb₂Se_{3-x} (or Sb₂Se₃) and the LiPS covering the full range of sulfur chemical states upon battery operation are depicted in Figure S8 (Supporting Information). The S–Sb and Li–Se attractions can be confirmed and are maintained in all the LiPS-adsorbent couples, while Sb₂Se_{3-x} exhibits stronger adsorbability for the LiPS by showing a constantly higher BE (Figure 4d) and a shorter bond length for both the S–Sb and Li–Se bonds (Figure 4e). In addition, we further performed calculations on a model in which three Se sites in the bulk layer were also removed (Bulk-Sb₂Se_{3-x}). As shown in Figure S9 (Supporting Information), this modification leads to even higher BEs between Sb₂Se_{3-x}

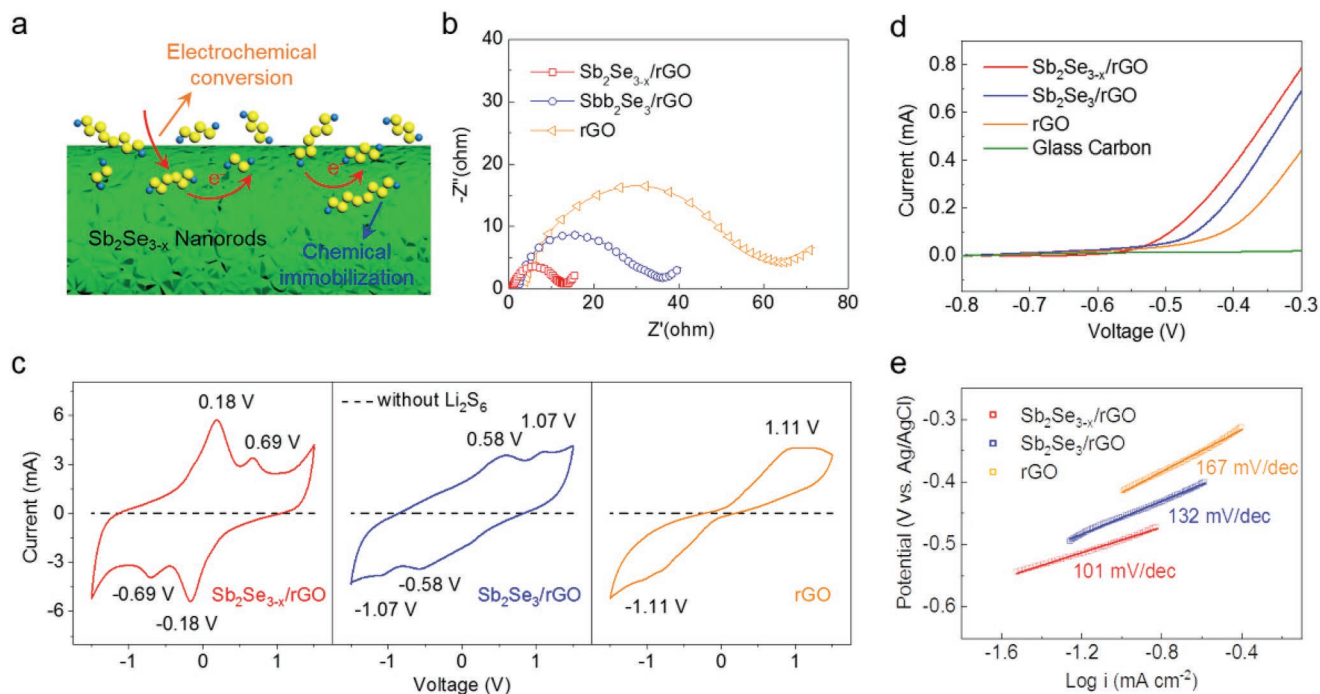


Figure 5. a) Schematic illustration of the LiPS conversion on the $\text{Sb}_2\text{Se}_{3-x}$ surface; b) EIS spectra and c) CV curves of symmetric cells with $\text{Sb}_2\text{Se}_{3-x}/\text{rGO}$, $\text{Sb}_2\text{Se}_3/\text{rGO}$ and rGO electrodes; d) LSV curves and e) Tafel plots of Li_2S oxidation on $\text{Sb}_2\text{Se}_{3-x}/\text{rGO}$, $\text{Sb}_2\text{Se}_3/\text{rGO}$ and rGO.

and polysulfides, further confirming the great capability of defect engineering in strengthening the polysulfide adsorption for sulfur electrochemistry.

In view of this, the obtained LiPS adsorbers were employed for the construction of a functional interlayer on a routine porous polypropylene membrane to evaluate their practical effect on polysulfide regulation. Figure S10 shows the basic information of the $\text{Sb}_2\text{Se}_{3-x}/\text{rGO}$ -modified separators. A distinct morphology difference can be observed between the routine and $\text{Sb}_2\text{Se}_{3-x}/\text{rGO}$ -modified separators, demonstrating the uniform coating of $\text{Sb}_2\text{Se}_{3-x}/\text{rGO}$, which is also confirmed by the homogeneous elemental mapping of C, Sb, and Se on the separator surface. The thickness of the $\text{Sb}_2\text{Se}_{3-x}/\text{rGO}$ coating was determined by cross-sectional SEM to be $\approx 32 \mu\text{m}$. The flexibility of the obtained $\text{Sb}_2\text{Se}_{3-x}/\text{rGO}$ -modified separator was also explored by a dynamic mechanical analysis (Q800, TA Instruments), as shown in Figure S11 (Supporting Information). The results show a well-maintained structural integrity upon repeated deformation with no fractures or peel-off, indicating the decent flexibility and considerable application potential of this separator in flexible devices.^[43] The LiPS diffusion behavior was investigated in an H-type cell configuration, where 0.1 M Li_2S_6 solution and a bare tetrahydrofuran (THF) solvent were separated by different separators, i.e., routine or that modified by rGO, $\text{Sb}_2\text{Se}_3/\text{rGO}$, or $\text{Sb}_2\text{Se}_{3-x}/\text{rGO}$. As contrastively shown in Figure 4f, the cell based on $\text{Sb}_2\text{Se}_{3-x}/\text{rGO}$ maintains a clear and transparent color in the opposite chamber, while the cell with the routine separator undergoes severe LiPS penetration that renders a dark brown color after 48 h. The LiPS diffusion based on the rGO- and $\text{Sb}_2\text{Se}_3/\text{rGO}$ -modified separators is also demonstrated in Figure S12 (Supporting Information), revealing a clear LiPS blocking strength order of

$\text{Sb}_2\text{Se}_{3-x}/\text{rGO} > \text{Sb}_2\text{Se}_3/\text{rGO} > \text{rGO} > \text{routine separator}$, benefiting from the strongest LiPS adsorption capability of $\text{Sb}_2\text{Se}_{3-x}/\text{rGO}$, consistent with the above results. The potent obstruction of LiPS diffusion by $\text{Sb}_2\text{Se}_{3-x}/\text{rGO}$ is expected to effectively suppress the shuttling behavior in the corresponding Li-S cells toward a stabilized sulfur electrochemistry.

In addition to sulfur confinement, the as-developed V_{Se} -rich $\text{Sb}_2\text{Se}_{3-x}/\text{rGO}$ could also serve as a promising electrocatalyst for the promotion of sulfur conversion due to its strong interaction with LiPSs as well as good charge transfer properties (Figure 5a). As proof of concept, symmetric cells were assembled using $\text{Sb}_2\text{Se}_{3-x}/\text{rGO}$, $\text{Sb}_2\text{Se}_3/\text{rGO}$ and rGO as identical electrodes and 0.2 M Li_2S_6 solution as the electrolyte to investigate the LiPS conversion kinetics on different surfaces. Figure 5b shows the electrochemical impedance spectroscopy (EIS) spectra of different symmetric cells. The $\text{Sb}_2\text{Se}_{3-x}/\text{rGO}$ symmetric cell clearly exhibits the lowest charge transfer resistance, suggesting its fast charge/mass transfer and facilitated sulfur redox reactions. Moreover, the cyclic voltammetry (CV) curves at a scanning rate of 10 mV s^{-1} of the different symmetric cells as well as those without the Li_2S_6 electrolyte are presented in Figure 5c. Two distinct pairs of redox peaks can be observed at $-0.18/0.18$ and $-0.69/0.69$ V for the $\text{Sb}_2\text{Se}_{3-x}/\text{rGO}$ cell, attributed to the multistep LiPS conversion reactions. In comparison, the CV curve of the $\text{Sb}_2\text{Se}_3/\text{rGO}$ cell exhibits a larger potential hysteresis with two broader redox peaks at $-0.58/0.58$ and $-1.07/1.07$ V, while the cell based on rGO suffers from even more severe polarization with only one pair of broad redox peaks at $-1.11/1.11$ V. This comparison strongly validates the smallest overpotential and fastest reaction kinetics for the LiPS conversion on the $\text{Sb}_2\text{Se}_{3-x}/\text{rGO}$ surface. Additionally, $\text{Sb}_2\text{Se}_{3-x}/\text{rGO}$ also exhibits the largest peak area

in the CV profile, further demonstrating its great capability for catalyzing the LiPS conversion and enhancing the sulfur utilization.^[44] Such a favorable catalytic effect also delivers decent durability, as confirmed by the well-overlapping CV profiles for several cycles (Figure S13, Supporting Information). In addition, the electrocatalytic activity of $\text{Sb}_2\text{Se}_{3-x}/\text{rGO}$ toward Li_2S oxidation was also evaluated in comparison with those of glass carbon, rGO, and $\text{Sb}_2\text{Se}_3/\text{rGO}$ through linear sweep voltammetry (LSV) measurements. The LSV was performed in a three-electrode configuration with 0.1 M Li_2S /methanol solution as the electrolyte, platinum sheet as the counter electrode and Ag/AgCl as the reference electrode. As shown in Figure 5d, $\text{Sb}_2\text{Se}_{3-x}/\text{rGO}$ delivers the lowest onset potential of -0.58 V (vs -0.53 and -0.50 V for $\text{Sb}_2\text{Se}_3/\text{rGO}$ and rGO, respectively) at a scanning rate of 10 mV s^{-1} and the highest current response among these modified separators, implying the lowest energy barrier to the Li_2S oxidization conversion and confirming the superior catalytic activity of the V_{Se} -rich $\text{Sb}_2\text{Se}_{3-x}/\text{rGO}$.^[45] This statement can be further supported by Tafel plot analysis of the Li_2S oxidization, which reveals a much smaller Tafel slope of $101 \text{ mV per decade}$ for $\text{Sb}_2\text{Se}_{3-x}/\text{rGO}$ compared with those for $\text{Sb}_2\text{Se}_3/\text{rGO}$ ($132 \text{ mV per decade}$) and rGO ($167 \text{ mV per decade}$), confirming the significant kinetic enhancement due to the defect-rich design (Figure 5e). In addition, the climbing-image nudged elastic band (CI-NEB) method was applied to study the kinetic process of Li_2S decomposition. The initial structure (IS), transition structure (TS), and final structure (FS) are given in Figure S14 (Supporting Information). The Li_2S decomposition has a much lower energy barrier of 0.46 eV on the V_{Se} -rich $\text{Sb}_2\text{Se}_{3-x}$ surface than that on pristine Sb_2Se_3 (0.91 eV), indicating the facilitated Li_2S transformation kinetics due to the existence of V_{Se} . All these results strongly demonstrate the superior catalytic activity of the V_{Se} -rich $\text{Sb}_2\text{Se}_{3-x}/\text{rGO}$ toward expedited LiPS conversion.

To explore the important roles of the functionalized separators in the electrochemical improvement of Li-S batteries, CR2032-type coin cells with different separators were assembled and evaluated. A S/CNT composite was prepared as the cathode material with a sulfur content of $\approx 71 \text{ wt\%}$, as determined by thermogravimetric analysis (TGA; Figure S15, Supporting Information). Figure 6a shows the initial CV curves of the cell with the $\text{Sb}_2\text{Se}_{3-x}/\text{rGO}$ -modified separator, which illustrates a typical two-step sulfur reduction upon cathodic scanning. The reduction peak at 2.31 V (vs Li/Li^+ , hereinafter inclusive) is associated with the reduction of S_8 to soluble long-chain LiPSs (Li_2S_n , $4 \leq n \leq 8$), while the peak at 2.10 V is assigned to the further reduction to insoluble $\text{Li}_2\text{S}_2/\text{Li}_2\text{S}$.^[46,47] The anodic scanning presents one oxidation peak at 2.34 V , corresponding to the conversion of $\text{Li}_2\text{S}/\text{Li}_2\text{S}_2$ back to Li_2S_n and S_8 .^[48,49] Such CV profiles overlap well during the initial several cycles, implying good cyclic stability and high reversibility of the sulfur redox reactions. Moreover, the CV curves of the cells with routine and rGO-, $\text{Sb}_2\text{Se}_3/\text{rGO}$ - and $\text{Sb}_2\text{Se}_{3-x}/\text{rGO}$ -modified separators are also compared in Figure S16 (Supporting Information). Clearly, the $\text{Sb}_2\text{Se}_{3-x}/\text{rGO}$ -modified separator enables the smallest electrochemical polarization and highest redox peak intensity among the different cells, indicating facilitated redox reactions and enhanced sulfur utilization.^[50] The galvanostatic charge–discharge profile at 0.1 C shows two

discharge plateaus and a charging slope in Figure 6b, which is consistent with the CV results according to the multistep sulfur reaction mechanism. Notably, the $\text{Sb}_2\text{Se}_{3-x}/\text{rGO}$ cell maintains the voltage profile well, with a small potential hysteresis over 100 cycles, suggesting inhibited LiPS shuttling and stabilized sulfur electrochemistry.

The galvanostatic cycling performances of the cells with different separators are presented in Figure 6c. The $\text{Sb}_2\text{Se}_{3-x}/\text{rGO}$ -modified separator enables a remarkable initial capacity of 1387 mAh g^{-1} at 0.1 C ($1 \text{ C} = 1675 \text{ mA g}^{-1}$), which is much higher than those based on the other separators (1249 , 1187 , and 1053 mAh g^{-1} for the $\text{Sb}_2\text{Se}_3/\text{rGO}$, rGO and routine separators, respectively), indicating significantly enhanced sulfur utilization. Additionally, a high capacity retention of 81.1% and a coulombic efficiency close to 100% over 100 cycles can also be obtained for the $\text{Sb}_2\text{Se}_{3-x}/\text{rGO}$ cell, strongly demonstrating its superior cycling stability over those of the other separator designs. The significant improvement in battery cyclability is attributed to the strong chemical interaction of the V_{Se} -rich $\text{Sb}_2\text{Se}_{3-x}/\text{rGO}$, as verified above, which establishes a powerful barrier against LiPS diffusion across the separator, resulting in efficient inhibition of LiPS shuttling. Figure 6d compares the rate performances of the different cells from 0.2 C to 8.0 C . The $\text{Sb}_2\text{Se}_{3-x}/\text{rGO}$ cell exhibits the best rate capability with a high capacity of 1249 mAh g^{-1} at 0.2 C and 787 mAh g^{-1} at 8.0 C . When switched back to 0.2 C , the capacity recovers to 1168 mAh g^{-1} , corresponding to 93.5% of its initial value. In comparison, the cells with the routine, rGO-modified and $\text{Sb}_2\text{Se}_3/\text{rGO}$ -modified separators undergo rapid capacity fading to low capacities of 56 , 161 and 377 mAh g^{-1} , respectively, at 8.0 C . The corresponding charge–discharge curves under different current densities are presented in Figure S17 (Supporting Information). The cell based on the $\text{Sb}_2\text{Se}_{3-x}/\text{rGO}$ -modified separator maintains the typical voltage profile even at a high rate up to 8.0 C , while the other separators, particularly the rGO and routine ones, suffer severe profile deformation upon an increase in the current rate. This electrochemical polarization behavior can also be perceived from the potential gap variation with the current rate for the different cells (Figure S18, Supporting Information). The superb rate capability benefits from the high conductivity and great catalytic activity of $\text{Sb}_2\text{Se}_{3-x}/\text{rGO}$ toward LiPS conversion, which significantly lowers the electrochemical resistance and improves the overall sulfur redox reaction kinetics. Additionally, Nyquist plots of the cells with different separators were also collected to study the enhancement of the kinetic reaction (Figure S19, Supporting Information). The plots consist of a semicircle and an inclined straight line corresponding to the charge transfer resistance (R_{ct}) and Warburg impedance, respectively. The cell with the $\text{Sb}_2\text{Se}_{3-x}/\text{rGO}$ -modified separator delivers the smallest ohmic resistance and charge transfer resistance as well as the steepest Warburg slope, indicating the beneficial enhancement of the electron/ion conductivity and ion diffusion due to the V_{Se} -rich $\text{Sb}_2\text{Se}_{3-x}/\text{rGO}$ design.

In view of the above results, the prolonged cycling behavior was further explored, as depicted in Figure 6e. The highly defective $\text{Sb}_2\text{Se}_{3-x}/\text{rGO}$ shows an excellent cyclability, retaining a high reversible capacity of 847 mAh g^{-1} after 500 cycles at 1.0 C , which corresponds to a minimum capacity

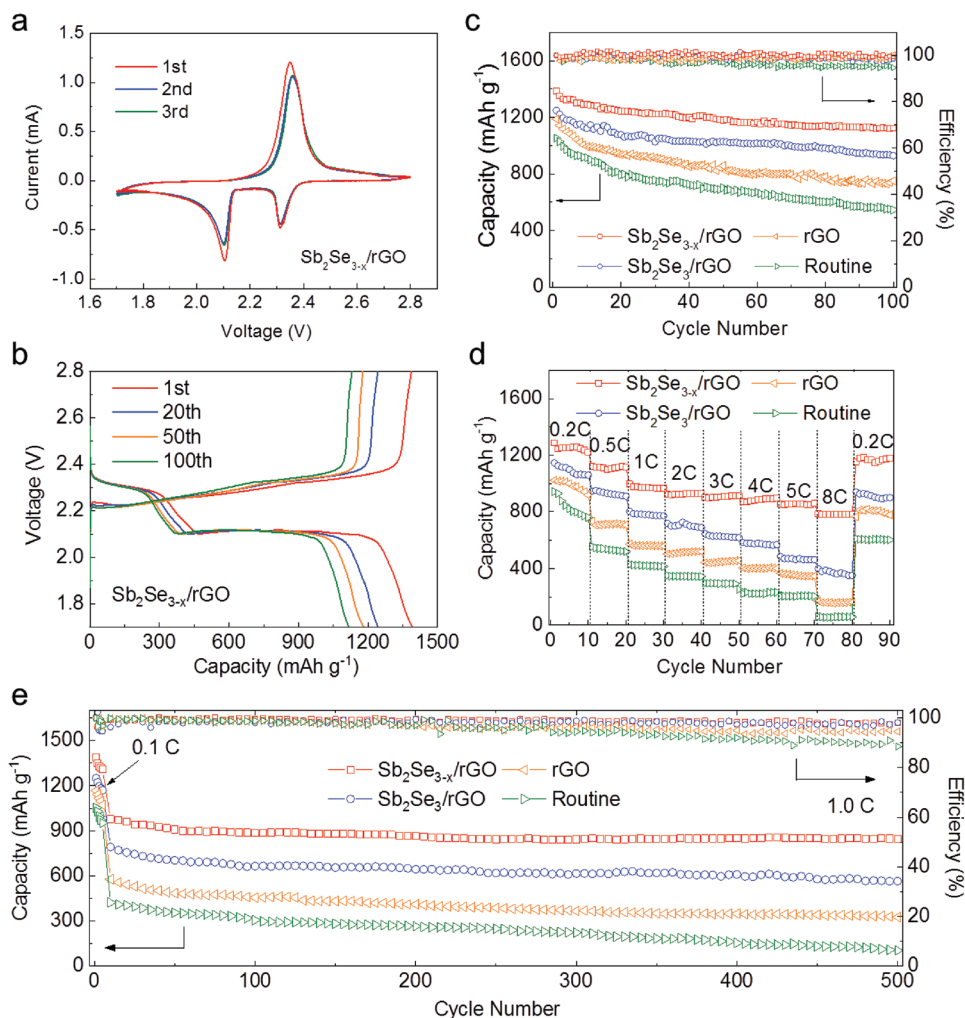


Figure 6. a) CV curves and b) charge–discharge profiles of the cell with the $\text{Sb}_2\text{Se}_{3-x}/\text{rGO}$ -modified separator; c) cycling performances at 0.1 C, d) rate performances, and e) prolonged cycling behavior at 1.0 C of cells with $\text{Sb}_2\text{Se}_{3-x}/\text{rGO}$ -, $\text{Sb}_2\text{Se}_3/\text{rGO}$ - and rGO-modified and routine separators with a sulfur loading of 1.8 mg cm^{-2} .

fading rate of 0.027% per cycle. In contrast, the cells with the routine, rGO-modified and $\text{Sb}_2\text{Se}_3/\text{rGO}$ -modified separators suffer from poorer capacity retention, with 104, 326, and 565 mAh g^{-1} capacities, respectively, after 500 cycles. These performances achieved by $\text{Sb}_2\text{Se}_{3-x}/\text{rGO}$ also reveal great competitiveness with the recently reported works based on functional interlayer design (Table S3, Supporting Information), which further demonstrates the great superiority of such defect engineering for battery improvement. These enhancements in the capacity, rate capability and cyclability are attributed to the highly conductive nature, rapid ion/mass transfer, and good LiPS affinity of the as-developed $\text{Sb}_2\text{Se}_{3-x}/\text{rGO}$, which immobilizes LiPS species and effectively catalyzes their electrochemical conversion, leading to active suppression of the shuttle effect and the resultant improvement in the battery performance. Additionally, the cycling performances based on $\text{Sb}_2\text{Se}_{3-x}/\text{rGO}$ with different defect levels were also compared, as shown in Figure S20 (Supporting Information). 5- $\text{Sb}_2\text{Se}_{3-x}/\text{rGO}$ enables the highest capacity and best cyclability, attributed

to its well-balanced V_{Se} content, structural integrity and conductivity.

In addition, the structural stability of the V_{Se} -rich $\text{Sb}_2\text{Se}_{3-x}/\text{rGO}$ design upon the charge–discharge process was further investigated by postmortem studies. The XRD patterns of $\text{Sb}_2\text{Se}_{3-x}/\text{rGO}$ before and after 100 cycles clearly illustrate the well-retained crystalline footprint (Figure S21, Supporting Information), manifesting its good structural stability during cell operation. Moreover, Se 3d XPS spectra of $\text{Sb}_2\text{Se}_{3-x}/\text{rGO}$ before and after 100 cycles were also recorded and compared with that of pristine Sb_2Se_3 , as presented in Figure S22 (Supporting Information). After 100 cycles, a new peak emerges at 53.1 eV, ascribed to the chemical bonding between Se and Li, which is consistent with the DFT calculation result.^[51] Moreover, the Se^0 peak of $\text{Sb}_2\text{Se}_{3-x}/\text{rGO}$ is retained, with a shift to a higher BE of 57.5 eV, indicating the well-maintained V_{Se} during the interaction with LiPSs during cell cycling.^[52] Therefore, the defective nature of $\text{Sb}_2\text{Se}_{3-x}/\text{rGO}$ can be well maintained upon battery operation, which constantly suppresses the shuttle

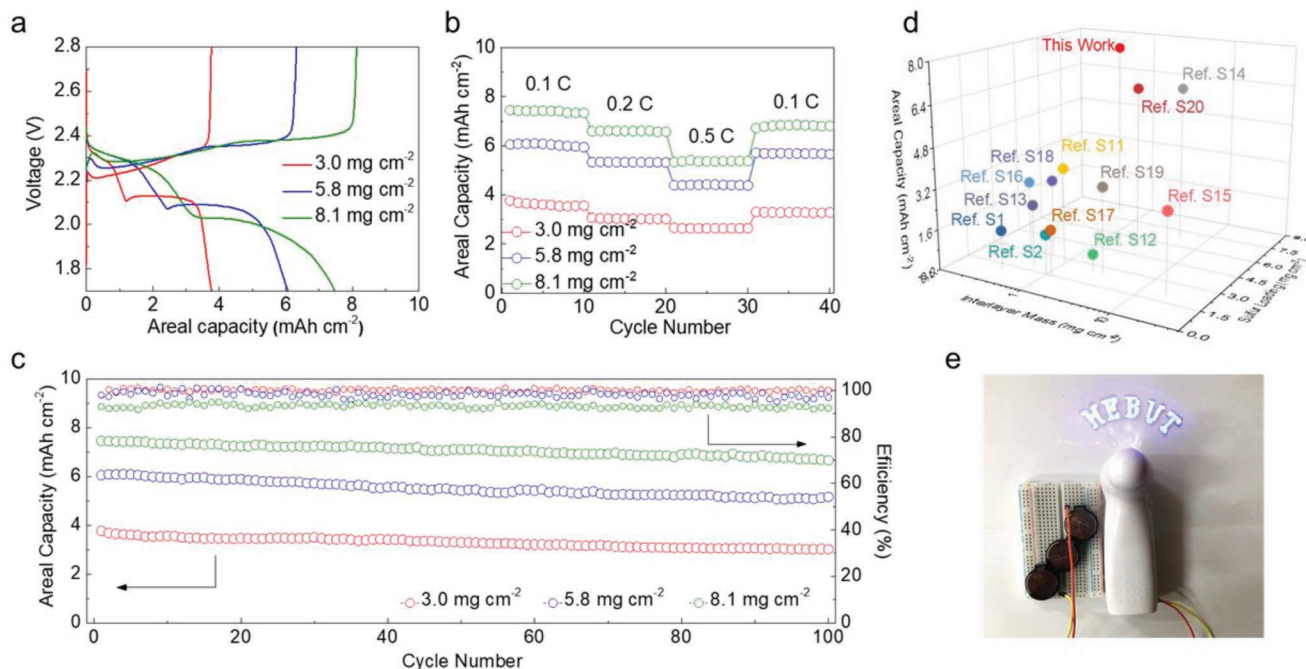


Figure 7. a) Charge–discharge profiles, b) rate performances, and c) cycling performances at 0.1 C of cells with $\text{Sb}_2\text{Se}_{3-x}/\text{rGO}$ -modified separators under raised sulfur loadings; d) performance comparison between cells with different separators; e) photograph of an electric fan with an “HEBUT” pattern powered by cells with the $\text{Sb}_2\text{Se}_{3-x}/\text{rGO}$ -modified separator.

effect and promotes the sulfur redox reactions for fast and durable sulfur electrochemistry.

Considering the potential application of Li–S batteries, studying the electrochemical performances under high areal sulfur loading to pursue a higher energy density beyond the material level is significant. Therefore, the as-developed $\text{Sb}_2\text{Se}_{3-x}/\text{rGO}$ -modified separator was implemented with raised sulfur loadings of 3.0, 5.8, and 8.1 mg cm^{-2} for further electrochemical evaluations. As shown in **Figure 7a**, a distinct two-plateau voltage profile is still achievable under high sulfur loading up to 8.1 mg cm^{-2} , with a high areal capacity of 7.46 mAh cm^{-2} . Additionally, the rate performances of $\text{Sb}_2\text{Se}_{3-x}/\text{rGO}$ -based cells under raised sulfur loadings are also depicted in **Figure 7b**. Decent areal capacities of 2.64, 4.43, and 5.39 mAh cm^{-2} can be retained under sulfur loadings of 3.0, 5.8, and 8.1 mg cm^{-2} , respectively, at a raised rate of 0.5 C, demonstrating the good capability of this V_{Se} -rich $\text{Sb}_2\text{Se}_{3-x}/\text{rGO}$ design in realizing low polarization and fast sulfur reaction kinetics under high-loading configurations. Furthermore, the cycling performances of the high-loading cells were evaluated, as shown in **Figure 7c**. Stable cycling behavior can be achieved based on the $\text{Sb}_2\text{Se}_{3-x}/\text{rGO}$ -modified separator, with high capacity retention values of 3.02, 5.16, and 6.66 mAh cm^{-2} at sulfur loadings of 3.0, 5.8, and 8.1 mg cm^{-2} , respectively, after 100 cycles. The good cyclability is attributed to the favorable adsorptive and catalytic superiorities of the as-developed hierarchical, porous and defective $\text{Sb}_2\text{Se}_{3-x}/\text{rGO}$ microspheres, which establish a highly effective functional layer that obstructs LiPS diffusion and promotes the sulfur redox kinetics, enabling strong inhibition of LiPS shuttling and a prolonged battery lifespan. Notably, the obtained high-loading performance is also highly competitive with the

recent publications based on functional interlayers when taking the critical parameters of the interlayer thickness, mass loading and electrode sulfur loading into account (**Figure 7d**; Table S4, Supporting Information). This comparison further validates the great superiority of the $\text{Sb}_2\text{Se}_{3-x}/\text{rGO}$ design in pursuing high-performance Li–S batteries. As a demonstration, cells with $\text{Sb}_2\text{Se}_{3-x}/\text{rGO}$ were capable of powering an electric fan with a light pattern of “HEBUT” (**Figure 7e**), suggesting a decent energy storage capability as well as great promise in promoting the practical application of Li–S batteries.

In summary, we developed exquisite defect-rich $\text{Sb}_2\text{Se}_{3-x}/\text{rGO}$ microspheres through a facile spray-drying method, which were designed for the construction of an efficient multifunctional LiPS barrier toward superior Li/S performance. The hierarchical architecture establishes a conductive framework for electron/ion transfer, while the highly porous structure exposes abundant active interfaces for LiPS confinement and conversion. Moreover, defect engineering endows the as-developed $\text{Sb}_2\text{Se}_{3-x}/\text{rGO}$ with enhanced conductivity, LiPS adsorbability, and catalytic activity, thus establishing a highly effective functional layer that effectively suppresses polysulfide shuttling and promotes the sulfur redox kinetics in Li/S batteries. Attributed to these beneficial features, the implementation of the $\text{Sb}_2\text{Se}_{3-x}/\text{rGO}$ -modified separator delivers an excellent long-term cycling stability with a low capacity fading of 0.027% per cycle over 500 cycles, a remarkable rate capability up to 8.0 C, and a high areal capacity of 7.46 mAh cm^{-2} under raised sulfur loading. This work provides a new perspective on defect engineering toward the concurrent realization of adsorptive and catalytic functionalities in separators, holding great promise in the development of high-performance Li/S batteries.

Experimental Section

Preparation of Sb_2Se_{3-x}/rGO : First, 0.23 g antimony trichloride ($SbCl_3$, 99.9%, Aladdin) was dissolved into 100 mL triethylene glycol (TEG, 99%, Aladdin), while 0.24 g selenium powder (Se, 99%, Aladdin) was dissolved into a mixture of 10 mL thioglycolic acid (TGA, 80%, Aladdin) and 90 mL monoethanolamine (MEA, 99%, Aladdin). The two obtained solutions were poured into a three-necked flask with 0.2 g PVP and heated at 190 °C for 20 min under a nitrogen atmosphere. After cooling, the precipitate was washed and centrifuged to obtain Sb_2Se_3 nanorods. Second, 0.42 g Sb_2Se_3 and 105 mL GO (2 mg mL⁻¹) were mixed under vigorous stirring, spray-dried, and chemically reduced by hydrazine through a steam bath process at 100 °C for 12 h to obtain Sb_2Se_3/rGO composites. Finally, the defect-rich Sb_2Se_{3-x}/rGO was obtained by subjecting Sb_2Se_3/rGO to a thermal shock at 600 °C in a tube furnace for 5 min under an Ar atmosphere.

Physical Characterization: The crystalline structures of materials were analyzed by an XRD diffractometer (D/Max 2500 V/pc, Rigaku) with Cu K α radiation. The Raman spectra were collected using a Raman microscope (Thermo Scientific, Waltham) system. The EPR measurement of vacancies was conducted with an Endor spectrometer (Bruker A300) at 77 K. XPS spectra were obtained using a PHI 5000 Versa Probe system. The morphological and structural information was collected by SEM (JSM-7100F, JEOL) and TEM (JEM-2100F, JEOL).

Electrochemical Characterization: The sulfur/carbon nanotube (S/CNT) composite was prepared by the melt-impregnation method. Typically, CNT and sulfur powder were well ground in a weight ratio of 3:7 and heated at 155 °C for 12 h to obtain the S/CNT composite. Then, the sulfur composite was homogeneously mixed with Super P and polyvinylidene fluoride (PVDF) at a mass ratio of 8:1:1 in 1-methyl-2-pyrrolidinone (NMP) solution. The slurry was coated on aluminum foil and dried at 60 °C for 12 h to obtain the sulfur electrode. The sulfur loading for regular electrodes was 1.8 mg cm⁻², while higher loadings up to 8.0 mg cm⁻² were also prepared. The modified separator was prepared by a simple surface coating method, in which 90 wt% Sb_2Se_{3-x}/rGO microsphere composites and 10 wt% PVDF were mixed together in NMP and coated on the routine separator. The mass loading of the interlayer materials was controlled at 0.5 mg cm⁻². Separators modified by Sb_2Se_3/rGO and bare rGO were also prepared for comparison. CR2032-type coin cells were assembled in an Ar-filled glove box with the S/CNT cathode, modified separator, and lithium anode for the electrochemical evaluations. The electrolyte consisted of 1.0 M lithium bis(trifluoromethane sulfonyl) dissolved in 1,3-dioxolane (DOL) and 1,2-dimethoxyethane (DME) (1:1; v:v) with 1 wt% LiNO₃. The electrolyte additions were 15 and 10 μ L mg⁻¹ for regular and high-loading cells, respectively. An electrochemical workstation (Princeton, VersaSTAT 4) was adopted to collect CV curves at operating potentials of 1.7 to 2.8 V with a scanning rate of 0.1 mV s⁻¹ and EIS plots in the frequency range of 0.01 Hz to 100 kHz. Galvanostatic charge–discharge and rate capability tests were carried out on a Neware battery test station. The current and capacity were calculated based on the mass of sulfur.

Theoretical Calculation: The DFT calculation was carried out using the VASP package with the generalized gradient approximation (GGA) and the Perdew–Burke–Ernzerhof (PBE) exchange and correlation functional.^[53–55] A plane-wave cutoff of 400 eV was used. The Brillouin zone was integrated using Monkhorst–Pack sets of a $2 \times 2 \times 1$ k-point mesh. The Sb_2Se_3 (130) surface was modeled using a (2×3) unit cell. The vacuum height was set to 15 Å. During the calculations, the bottom two atomic layers were fixed, whereas the remaining layers and the adsorbents were allowed to relax. Structures were fully relaxed until the forces acting on the atoms were less than 0.03 eV Å⁻¹. The Sb_2Se_{3-x} (130) surface (containing selenium vacancies) was constructed by placing three selenium vacancies on the bridging selenium rows in the Sb_2Se_3 surface.^[56,57] The Sb_2Se_{3-x} (130) surface was built by removing three selenium sites on the topmost layer. The Li_2S_n ($n = 1, 2, 4, 6, 8$) adhesion bonding energy (E_b) was calculated as follows: $E_b = E_{Li_2S_n/Sb_2Se_{3-x}} - E_{Li_2S_n} - E_{Sb_2Se_{3-x}}$, where $E_{Li_2S_n/Sb_2Se_{3-x}}$, $E_{Li_2S_n}$, and $E_{Sb_2Se_{3-x}}$ represent the total energy of the system, isolated Li_2S_n polysulfide and Sb_2Se_{3-x} , respectively.

Supporting Information

Supporting Information is available from the Wiley Online Library or from the author.

Acknowledgements

Y.T. and G.L. contributed equally to this work. This work was supported by the Program for the Outstanding Young Talents of Hebei Province, China, Chunhui Project of Ministry of Education of the People's Republic of China (Grant No. Z2017010), National Natural Science Foundation of China (21908039), and Natural Science Foundation of Hebei Province (B2019202199). The authors also thank the great support from the Natural Sciences and Engineering Research Council of Canada (NSERC) and the University of Waterloo.

Conflict of Interest

The authors declare no conflict of interest.

Keywords

antimony selenide, catalytic conversion, lithium–sulfur batteries, modified separators, selenium vacancies

Received: July 30, 2019
Revised: October 16, 2019
Published online:

- [1] A. Manthiram, Y. Fu, S. H. Chung, C. Zu, Y. S. Su, *Chem. Rev.* **2014**, *114*, 11751.
- [2] S. Bai, X. Liu, K. Zhu, S. Wu, H. Zhou, *Nat. Energy* **2016**, *1*, 16094.
- [3] Z. W. She, Y. Sun, Q. Zhang, Y. Cui, *Chem. Soc. Rev.* **2016**, *45*, 5605.
- [4] D. Luo, G. Li, Y. Deng, Z. Zhang, J. Li, R. Liang, M. Li, Y. Jiang, W. Zhang, Y. Liu, W. Lei, A. Yu, Z. Chen, *Adv. Energy Mater.* **2019**, *9*, 1900228.
- [5] Q. Pang, X. Liang, C. Y. Kwok, L. F. Nazar, *Nat. Energy* **2016**, *1*, 16132.
- [6] K. Y. Xie, Y. You, K. Yuan, W. Lu, K. Zhang, F. Xu, M. Ye, S. M. Ke, C. Shen, X. R. Zeng, X. L. Fan, B. Q. Wei, *Adv. Mater.* **2017**, *29*, 1604724.
- [7] D. Lin, Y. Liu, Y. Cui, *Nat. Nanotechnol.* **2017**, *12*, 194.
- [8] M. Yan, H. Chen, Y. Yu, H. Zhao, C. F. Li, Z. Y. Hu, P. Wu, L. H. Chen, H. E. Wang, D. L. Peng, H. X. Gao, T. Hasan, Y. Li, B. L. Su, *Adv. Energy Mater.* **2018**, *8*, 1801066.
- [9] W. Chen, T. Y. Lei, T. Qian, W. Q. Lv, W. D. He, C. Y. Wu, X. J. Liu, J. Liu, B. Chen, C. L. Yan, J. Xiong, *Adv. Energy Mater.* **2018**, *8*, 1702889.
- [10] J. Zhang, C. P. Yang, Y. X. Yin, L. J. Wan, Y. G. Guo, *Adv. Mater.* **2016**, *28*, 9539.
- [11] M. Li, Y. Zhang, Z. Bai, W. W. Liu, T. Liu, J. Gim, G. Jiang, Y. Yuan, D. Luo, K. Feng, R. S. Yassar, X. Wang, Z. Chen, *Adv. Mater.* **2018**, *30*, 1804271.
- [12] G. Li, S. Wang, Y. Zhang, M. Li, Z. Chen, J. Lu, *Adv. Mater.* **2018**, *30*, 1705590.
- [13] C. Deng, Z. W. Wang, S. P. Wang, J. X. Yu, D. J. Martin, A. K. Nanjundan, Y. Yamauchi, *ACS Appl. Mater. Interfaces* **2019**, *11*, 541.
- [14] J. Balach, T. Jaumann, M. Klose, S. Oswald, J. Eckert, L. Giebeler, *Adv. Funct. Mater.* **2015**, *25*, 5285.

- [15] G. Li, D. Luo, X. Wang, M. H. Seo, S. Hemmati, A. Yu, Z. Chen, *Adv. Funct. Mater.* **2017**, *27*, 1702562.
- [16] J. Zhang, H. Hu, Z. Li, X. W. D. Lou, *Angew. Chem., Int. Ed.* **2016**, *55*, 3982.
- [17] W. Chen, T. Qian, J. Xiong, N. Xu, X. J. Liu, J. Liu, J. Q. Zhou, X. W. Shen, T. Z. Yang, Y. Chen, C. L. Yan, *Adv. Mater.* **2017**, *29*, 1605160.
- [18] X. Liang, C. Hart, Q. Pang, A. Garsuch, T. Weiss, L. F. Nazar, *Nat. Commun.* **2015**, *6*, 5682.
- [19] Y. C. Jeong, J. H. Kim, S. Nam, C. R. Park, S. J. Yang, *Adv. Funct. Mater.* **2018**, *28*, 1707411.
- [20] Z. Liang, G. Y. Zheng, W. Y. Li, Z. W. Seh, H. B. Yao, K. Yan, D. S. Kong, Y. Cui, *ACS Nano* **2014**, *8*, 5249.
- [21] Y. L. Zhang, Z. J. Mu, C. Yang, Z. K. Xu, S. Zhang, X. Y. Zhang, Y. J. Li, J. P. Lai, Z. H. Sun, Y. Yang, Y. G. Chao, C. J. Li, X. X. Ge, W. X. Yang, S. J. Guo, *Adv. Funct. Mater.* **2018**, *28*, 1707578.
- [22] X. S. Liu, J. Chen, M. Luo, M. Y. Leng, Z. Xia, Y. Zhou, S. K. Qin, D. J. Xue, L. Lv, H. Huang, D. M. Niu, J. Tang, *ACS Appl. Mater. Interfaces* **2014**, *6*, 10687.
- [23] R. Vadapoo, S. Krishnan, H. Yilmaz, C. Marin, *Nanotechnology* **2011**, *22*, 175705.
- [24] G. Ghosh, *J. Phase Equilib.* **1993**, *14*, 753.
- [25] S. Siebentritt, M. Igalson, C. Persson, S. Lany, *Prog. Photovoltaics* **1993**, *14*, 753.
- [26] Y. Tian, Z. H. Sun, Y. Zhao, T. Z. Tan, H. Liu, Z. H. Chen, *J. Nanomater.* **2018**, *2018*, 4273945.
- [27] J. Chen, Z. Ding, C. Wang, H. Hou, Y. Zhang, C. Wang, G. Zou, X. Ji, *ACS Appl. Mater. Interfaces* **2016**, *8*, 9142.
- [28] Z. Wang, C. Yang, T. Lin, H. Yin, P. Chen, D. Wan, F. Xu, F. Huang, J. Lin, X. Xie, M. Jiang, *Energy Environ. Sci.* **2013**, *6*, 3007.
- [29] Y. Wang, D. Z. Kong, W. H. Shi, B. Liu, G. J. Sim, Q. Ge, H. Y. Yang, *Adv. Energy Mater.* **2016**, *6*, 1601057.
- [30] Y. T. Zuo, G. Wang, J. Peng, G. Li, Y. Q. Ma, F. Yu, B. Dai, X. H. Guo, C. P. Wong, *J. Mater. Chem. A* **2016**, *4*, 2453.
- [31] J. Xiao, X. Chen, P. V. Sushko, M. L. Sushko, L. Kovarik, J. Feng, Z. Deng, J. Zheng, M. L. Graff, Z. Nie, D. Choi, J. Liu, J. G. Zhang, M. S. Whittingham, *Adv. Mater.* **2012**, *24*, 2109.
- [32] S. Balendhran, J. K. Deng, J. Z. Ou, S. Walia, J. Scott, J. S. Tang, K. L. Wang, M. R. Field, S. Russo, S. Zhuiykov, M. S. Strano, N. Medhekar, S. Sriram, M. Bhaskaran, K. Kalantar-zadeh, *Adv. Mater.* **2013**, *25*, 109.
- [33] H. S. Kim, J. B. Cook, H. Lin, J. S. Ko, S. H. Tolbert, V. Ozolins, B. Dunn, *Nat. Mater.* **2017**, *16*, 454.
- [34] Y. Sun, J. Meng, H. X. Ju, J. F. Zhu, Q. X. Li, Q. Zhang, *J. Mater. Chem. A* **2018**, *6*, 22526.
- [35] S. D. Setzler, M. Moldovan, Z. Yu, T. H. Myers, N. C. Giles, L. E. Halliburton, *Appl. Phys. Lett.* **1997**, *70*, 2274.
- [36] S. B. Zhang, J. E. Northrup, *Phys. Rev. Lett.* **1991**, *67*, 2339.
- [37] P. V. Prikhodchenko, J. Gun, S. Sladkevich, A. A. Mikhaylov, O. Lev, Y. Y. Tay, S. K. Batabyal, D. Y. W. Yu, *Chem. Mater.* **2012**, *24*, 4750.
- [38] L. Y. Xu, S. B. Qian, Y. Xie, E. X. Wu, H. C. Hei, Z. H. Feng, S. Wu, X. D. Hu, T. Guo, D. H. Zhang, *Nanotechnology* **2018**, *29*, 175703.
- [39] H. Yuan, H. J. Peng, B. Q. Li, J. Xie, L. Kong, M. Zhao, X. Chen, J. Q. Huang, Q. Zhang, *Adv. Energy Mater.* **2019**, *9*, 1802768.
- [40] G. Li, W. Lei, D. Luo, Y. Deng, Z. Deng, D. Wang, A. Yu, Z. Chen, *Energy Environ. Sci.* **2018**, *11*, 2372.
- [41] X. Liang, A. Garsuch, L. F. Nazar, *Angew. Chem., Int. Ed.* **2015**, *54*, 3907.
- [42] T. Z. Hou, W. T. Xu, X. Chen, H. J. Peng, J. Q. Huang, Q. Zhang, *Angew. Chem., Int. Ed.* **2017**, *56*, 8178.
- [43] F. X. Yin, J. Z. Yang, H. F. Peng, W. J. Yuan, *J. Mater. Chem. C* **2018**, *6*, 6840.
- [44] H. B. Lin, L. Q. Yang, X. Jiang, G. C. Li, T. R. Zhang, Q. F. Yao, G. Y. W. Zheng, J. Y. Lee, *Energy Environ. Sci.* **2017**, *10*, 1476.
- [45] S. F. Wang, X. H. Hou, Z. M. Zhong, K. X. Shen, G. Z. Zhang, L. M. Yao, F. M. Chen, *Sci. Rep.* **2018**, *8*, 16133.
- [46] J. Wang, C. Lv, Y. Zhang, L. Deng, Z. Peng, *Electrochim. Acta* **2015**, *165*, 136.
- [47] L. Ji, M. Rao, H. Zheng, L. Zhang, Y. Li, W. Duan, J. Guo, E. J. Cairns, Y. Zhang, *J. Am. Chem. Soc.* **2011**, *133*, 18522.
- [48] S. Moon, Y. H. Jung, W. K. Jung, D. S. Jung, J. W. Choi, D. K. Kim, *Adv. Mater.* **2013**, *25*, 6547.
- [49] M. C. Orilall, N. M. Abrams, J. Lee, F. J. DiSalvo, U. Wiesner, *J. Am. Chem. Soc.* **2008**, *130*, 8882.
- [50] L. L. Zhang, X. Chen, F. Wan, Z. Q. Niu, Y. J. Wang, Q. Zhang, *ACS Nano* **2018**, *12*, 9578.
- [51] Y. Wei, Y. Tao, Z. Kong, L. Liu, J. Wang, W. Qiao, L. Ling, D. Long, *Energy Storage Mater.* **2016**, *5*, 171.
- [52] R. Golovchak, O. Shpotyuk, A. Kovalskiy, A. C. Miller, J. Čech, H. Jain, *Phys. Rev. B* **2008**, *77*, 172201.
- [53] J. P. Perdew, K. Burke, M. Ernzerhof, *Phys. Rev. Lett.* **1996**, *77*, 3865.
- [54] G. Kresse, J. Hafner, *Phys. Rev. B* **1993**, *47*, 558.
- [55] G. Kresse, J. Furthmüller, *Phys. Rev. B* **1996**, *54*, 11169.
- [56] R. Zhang, B. Wang, H. Liu, L. Ling, *J. Phys. Chem. C* **2011**, *115*, 19811.
- [57] Y. Pan, C. Liu, Q. Ge, *J. Catal.* **2010**, *272*, 227.